China Instrument and Control Society
Instrumentation
OPEN ACCESS
INSTRUMENTATION, Vol. 12, No. 3, September 2025 https://doi.org/10.15878/j.instr.202500301

Article

A Wideband High-Gain Antenna for Low-Altitude UAV Airspace Control

Bing Yu[1,2*], Xiaoxin Yang[1*], Fei Liu[3], Jiang Shang[1], Yan Li[1]

[1] School of Electronics & Information Engineering, Nanjing University of Information Science & Technology, Nanjing 210044, China

[2] Jiangsu Atmospheric Environment and Equipment Technology Collaborative Innovation Center, Nanjing 210044, China

[3] Science and Technology Information Bureau, Hangzhou Municipal Public Security Bureau, Hangzhou 310000, China

[*] Corresponding author email: 202312490135@nuist.edu.cn

Abstract: This paper proposes a portable broadband high-gain antenna for unmanned aerial vehicle (UAV) low-altitude control, operating within the dedicated remotely piloted aircraft system (RPAS) band (5.03–5.91 GHz). The total size of the antenna is 240×240×187 mm^3. It uses a printed log-periodic dipole antenna (PLPDA) as feed, and a four-layer frequency selective surface (FSS) cascaded as radome to enhance gain. Experimental results demonstrate that the antenna gain ranges from 10.1 to 15.9 dB and the half-power beam width (HPBW, $2\theta_{0.5}$) <23° within the operation band. Compared to existing portable UAV low-altitude control systems, the proposed antenna achieves an average gain enhancement of 4.7 dB.

Keywords: unmanned aerial vehicle (UAV); low-altitude control; antenna; frequency selective surface (FSS)

Citation: Bing Yu, Xiaoxin Yang, Fei Liu, Jiang Shang, Yan Li."A Wideband High-Gain Antenna for Low-Altitude UAV Airspace Control." Instrumentation 12, no.3 (September 2025). https://doi.org/10.15878/j.instr.202500301

1 Introduction

With the advent of intensified exploitation and utilization of low-altitude airspace resources, there has been an explosive growth in the application of unmanned aerial vehicles (UAVs) across diverse domains such as logistics, inspection, aerial photography, and emergency response. While the widespread deployment of UAVs significantly enhances socio-economic efficiency, it concurrently precipitates increasingly critical challenges in low-altitude control. Particularly for sensitive airspace zones, major event security operations, and critical infrastructure protection, flexible configuration and low-cost counter-drone technologies has become an urgent priority[1-5].

Existing low altitude control system (LACS), predominantly based on fixed base stations or radar, exhibit limited effectiveness against "low-slow-small" (LSS) UAVs (operating altitude <1000 m, speed <200 km/h, radar cross-section <2 m^2) and with high cost, large response latency, and poor deployment flexibility, which render them inadequate for meeting the demands of emergent and mobile counter-drone operations. In contrast, the portable LACS demonstrate distinct advantages in scenarios requiring immediate intervention or point defense, attributable to their high mobility and rapid response capabilities[6]. These systems can not only be implemented in portable jamming guns due to their compact size, but also extend jamming range through aerial-mounted platforms.

Recent advances in portable LACS include: Ikhwan Kim et al.[7]proposed a broadband gain enhanced narrow beam Vivaldi antenna with directors for a portable LACS. This antenna covers GPS L1, ISM 2.4 GHz, ISM 5.8 GHz, and the remotely piloted aircraft system (RPAS) band (5.03 – 5.91 GHz), with a measured peak gain of 10 dB and the $2\theta_{0.5}$ of 20.9° . Wang et al. [8]developed a miniaturized portable UAV interference antenna operating at 1575.42±1.023 MHz, 2.4–2.5 GHz, and 5.6–5.8 GHz. Test results demonstrate that the gain reaches 10.3 dBi within 1.57 – 1.58 GHz, 9 dBi within 2.4 – 2.5 GHz, and 10 dBi within 5.6 – 5.8 GHz, respectively. Xie et al. [9]introduced a dual-band dual-feed UAV

interference antenna operating at 1570 – 1580 MHz and 2400 – 2500 MHz. The designed antenna achieves a gain of 10 dB within the target bands, while exhibiting a $2\theta_{0.5}$ of approximately 40° at 2.4 GHz. Based on the above literature analysis, two critical factors must be considered for jamming antenna design in portable LACS:

1. Multi-band miniaturization: The antenna should cover key UAV operating bands—GPS L1, ISM 2.4 GHz, ISM 5.8 GHz, and RPAS (5.03 – 5.91 GHz) —while maintaining compact dimensions and lightweight construction.

2. High gain is essential to achieve effective long-range jamming signals, supported by fixed LACS implementations where 15-dBi Yagi-Uda antennas achieve only 380 meters of jamming distance at 2.4 GHz[10].

Concurrently, narrow $2\theta_{0.5}$ must be ensured for precise target discrimination and minimal collateral interference. The synergy of broad bandwidth and high gain constitutes the core bottleneck in extending the effective control range of portable counter-UAV systems.

In order to solve the problems mentioned above, in this paper, we optimise the performance of the antenna used in portable LACS by using an antenna radome. The radome integrates a novel design of heterogeneous FSS units, constructed by cascading four layers, which has not been previously reported in the literature. This configuration achieves 360° broad transmission phase coverage within the 5.03–5.91 GHz frequency band, with a transmission loss of less than 1 dB. Meanwhile, within a compact volume of 240×240×187 mm³, it effectively increases the antenna gain and reduces the $2\theta_{0.5}$ beamwidth.

2 Antenna Radome Design

The proposed antenna comprises two components: a feed antenna and a radome. Specifically, the feed antenna employs a printed log-periodic dipole antenna (PLPDA), which reduces both weight and volume compared to horn-fed jamming antennas[11,12], thereby offering better suitability for portable applications. The radome is constructed of a four-layer cascaded FSS structure, where each FSS layer integrates two distinct low-transmission-loss heterogeneous elements, which are named UC1 and UC2, respectively. Modeling and optimization of these elements were conducted using an equivalent circuit model (ECM) approach.

2.1 Radome Unit Cell Design

To achieve the wideband characteristics of RPAS, an ECM is adopted for designing wideband radome unit cells, as illustrated in Fig. 1, where the hybrid resonator consists of a parallel combination of an inductor and a series LC resonator. The reasons for choosing this ECM are as follows: 1) its commonality and universality in literature[13-15]; 2) it has many mapping unit topologies; 3) the formulas deriving circuit parameters from the desired

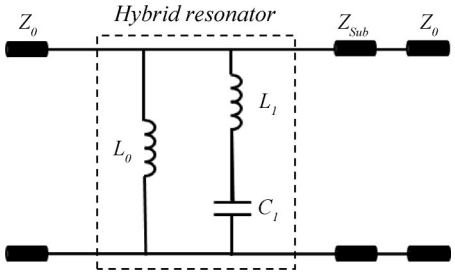

Fig.1 Equivalent circuit of radome unit cell.

frequency response have been proposed in literature[13]. The ECM can produce a transmission zero f_z and a transmission pole f_p:

$$f_z = \frac{1}{2\pi\sqrt{L_1 C_1}} \tag{1}$$

$$f_p = 2\pi f_z \sqrt{\frac{1}{C_1 L_0 (2\pi f_z)^2 + 1}} \tag{2}$$

After establishing the ECM, the corresponding radome unit cell structure can be derived.

Fig. 2 illustrates the three-dimensional structure of UC1 of the radome. The metal layer in Fig. 2(a) is supported by an F4B substrate (relative permittivity = 2.65, loss tangent = 0.001) with a thickness h = 1 mm. The metal layer of which comprises an external square ring and an internal central connecting structure: the external square ring (length P, width t) is modeled as an inductor L_0, while the internal arm-like structure (length D_1, width a) is modeled as a strip inductor L_1. The gap between the square ring edge and the internal arm (width b) forms a capacitance C_1. The characteristic impedance of the dielectric substrate Z_{sub} is negligible due to its ultra-thin thickness h[16]Fig. 3(a) demonstrates a comparison of the S-parameters obtained through full-wave simulation and the equivalent circuit method. It is observed that both the reflection coefficient S_{11} and the transmission coefficient S_{21} exhibit excellent agreement, validating that UC1 is designed to resonate at 5.8 GHz with broadband characteristics. Furthermore, the S_{21} results in Fig. 3(a) indicate that the transmission loss of UC1 for electromagnetic waves is < 1 dB at the resonant frequency.

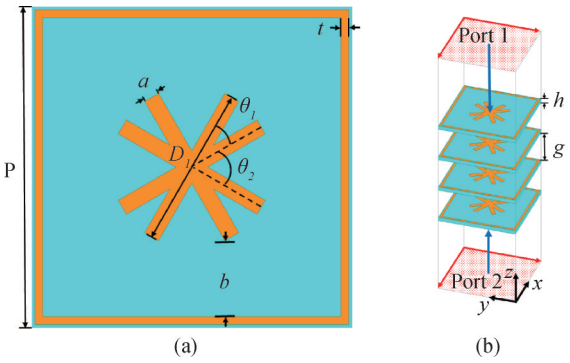

Fig.2 The proposed UC1 and its simulated setup. (a) Top view; (b) Perspective view.

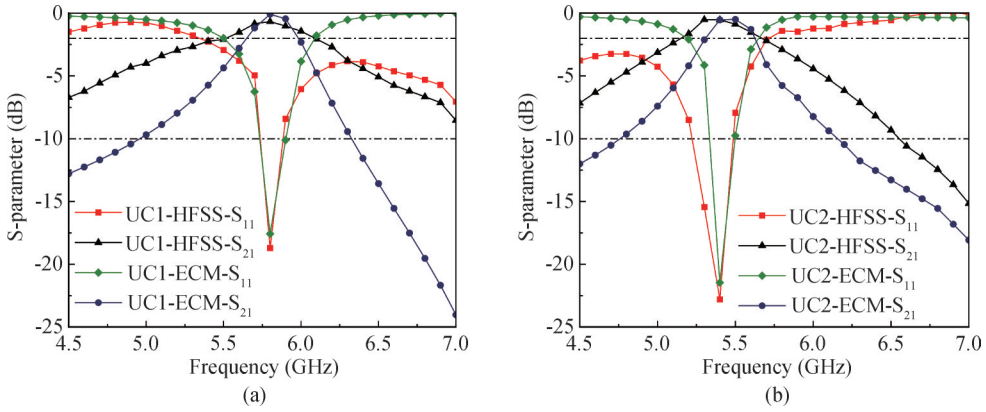

Fig.3 Performance comparison between full-wave simulation and equivalent circuit (a) UC1. (b) UC2.

In order to ensure that the radome unit cells can cover 360° full phase adjustment capability, the structure shown in Fig.2(b) is cascaded[17]. As shown in this figure, UC1 comprises four metallic radiating layers, four dielectric layers, and three air gaps with a thickness g = 8 mm. Following optimization via ECM, the key design parameters for the UC1 metal layer were determined as follows: square ring length P = 20 mm, ring width t = 0.5 mm, gap b = 3.9mm and center connecting component width a = 1 mm. To ensure broadband operation and low transmission loss, parametric optimization was performed on the inter-dipole angles (θ_1, θ_2), resulting in optimal angles of θ_1 = 30° and θ_2 = 60° . By varying the dipole arm length D_1, the phase of electromagnetic waves transmitted through UC1 can be tuned.

Full-wave simulations employing periodic boundaries in both x- and y- directions were conducted on the four-layer cascaded UC1 structure as shown in Fig. 2 (b). As denoted in Fig.4(a), when D_1 ranges from 10 to 14 mm, the transmission loss remains substantially below 1 dB within 5 – 6GHz, confirming its broadband low-loss characteristics within the RPAS band. The phase tuning range as shown in Fig. 4(b) achieves 360° coverage at 6 GHz and 324° at 5.8 GHz, while maintaining 237° at the lower band edge of 5 GHz. These results indicate that UC1 satisfies the < -1 dB transmission loss requirement but fails to achieve 360° phase coverage across the operational bandwidth.

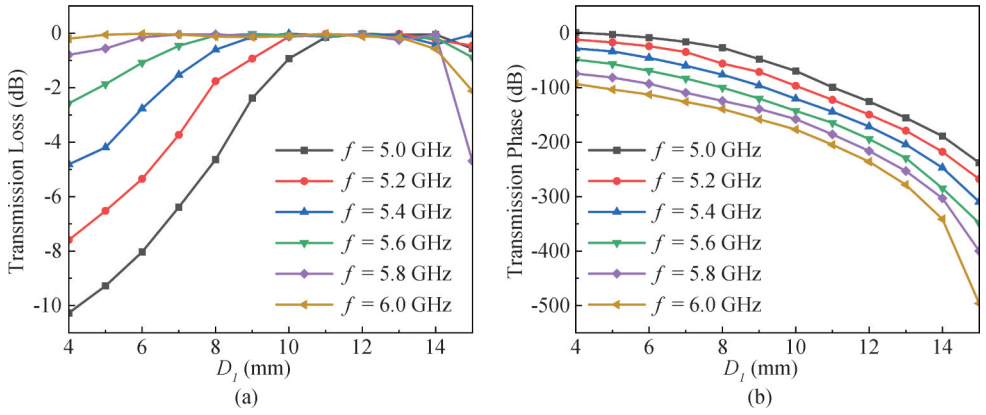

Fig.4 Simulated transmission coefficient of the UC1 (a) Loss (b) Phase

To address the limitations of UC1 in the RPAS band regarding transmission phase and transmission loss, we propose UC2 based on the equivalent circuit model (ECM) in Fig. 1 and building upon the UC1 design. Fig.5 depicts the three-dimensional structure of UC2 of the radome. As shown in Fig. 5(a), the most significant difference from UC1 lies in the central connecting part: the metallic layer of UC2 adopts a composite design consisting of a square loop embedded with cross-shaped arms and arc-shaped patches. This reconfiguration of the central component (corresponding to inductor L_1) enables adjustment of the unit cell's resonant frequency. Fig. 3(b) compares the S-parameters of UC2 obtained through full-wave simulation and the equivalent circuit method. The reflection coefficient S_{11} and transmission coefficient S_{21} demonstrate strong consistency across both methodologies, validating the accuracy of the equivalent circuit approach. UC2 resonates at 5.4 GHz with broadband characteristics, maintaining transmission loss below 1 dB across the operational bandwidth.

Consistent with UC1, parametric optimization was applied to the angle θ_3 to ensure broadband operation and low transmission loss, yielding an optimal θ_3 = 32° . Varying the cross-arm length D_2 enables transmission phase tuning of UC2. Full-wave simulations with periodic boundaries in both x- and y- directions were

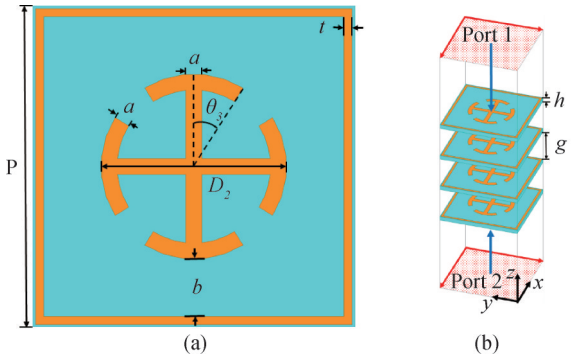

Fig.5 The proposed UC2 and its simulated setup
(a) Top view; (b) Perspective view

performed on the four-layer cascaded UC2 structure as shown in Fig.5(b). The transmission loss results presented in Fig. 6(a) reveal that when D_2 varies between 11.0 mm and 11.5 mm, UC2 exhibits a further reduction in transmission loss compared to UC1, demonstrating enhanced electromagnetic wave transmission efficiency. Fig. 6(b) indicates a transmission phase tuning range of 80° to 152° for UC2 within the RPAS band, which confirms that by adopting a phase-complementary design integrating UC1 and UC2, the radome achieves < 1 dB transmission loss concurrently with a 360° continuous phase tuning range covering the RPAS operational band.

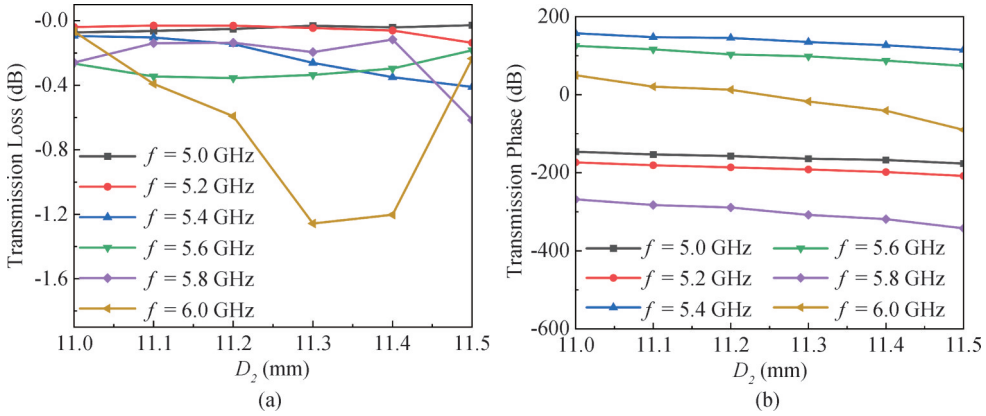

Fig.6 Simulated transmission coefficient of the UC2. (a) Loss. (b) Phase

2.2 Radome Design

Fig.7 illustrates the operational principle of the FSS-based radome, where the feed antenna is equivalent to an ideal point source located in the near-field region of the radome. To improve the gain, we convert the spherical wavefront radiated by the feed antenna into a planar wavefront via the radome. To realize the wavefront conversion, each radome unit cell provides a transmission phase shift that compensates for the spatial path delay caused by varying propagation distances from the feed's phase center. The required compensation phase φ_i for the i-th unit cell is given by:

$$\varphi_i = k(R_i - r_i \cdot \hat{r}_0) + \varphi_0 \tag{3}$$

where k denotes the free-space wavenumber, R_i represents the distance from the feed's phase center to the i-th cell, r_i is the position vector of the i-th cell, r_0 indicates the main beam direction, and φ_0 is a constant reference phase for radome design. Since $k = 2\pi f\sqrt{\mu\varepsilon}$ is a linear function of frequency, $\varphi_i$exhibits inherent frequency dependence. Consequently, the transmission phase of each unit cell is jointly determined by its phase value $\varphi_i(f_0)$ at the center frequency f_0 and its phase slope across the band, imposing significant design challenges in simultaneously fulfill both requirements. In this work, f_0 is set to 5.8 GHz, and the phase compensation is designed solely based on $\varphi_i(f_0)$ at this frequency. Combined with Eq. (3), Fig. 8 depicts the phase compensation distribution across the proposed radome.

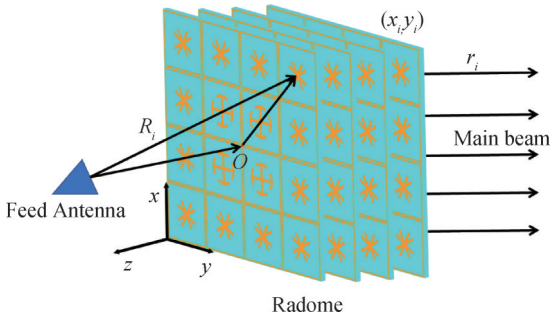

Fig.7 Schematic view of the wideband radome

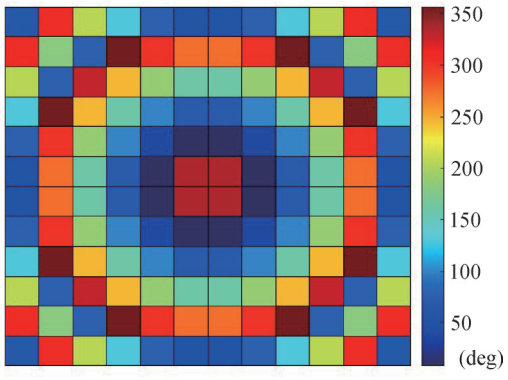

Fig.8 Phase compensation distribution across the proposed radome

2.3 Portable LACS Antenna Design

The proposed antenna employs a PLPDA as a feed, with a detailed structure illustrated in Fig. 9(a). The PLPDA geometry conforms to the specific scaling relationship equation:

$$\frac{l_1}{l_2} = \frac{w_2}{w_3} = \tau \tag{4}$$

The feed antenna utilizes a 1.6-mm-thick FR4 substrate (relative permittivity = 4.4, loss tangent = 0.02). To ensure effective impedance matching to a 50-Ω SMA connector, the feedline width is designed as 3 mm, and other detailed PLPDA parameters are listed in Table 1.

Table 1 Design Parameters of the PLPDA (Unit: mm).

τ	l	w	l_1	l_2	l_3	l_4	l_5	l_6	l_7	l_8
0.824	64.00	72.50	9.29	11.27	13.67	16.60	20.15	24.45	29.67	36.01
l_9	l_{10}	w_1	w_2	w_3	w_4	w_5	w_6	w_7	w_8	w_9
43.70	3.00	12.82	3.30	4.00	4.86	5.90	7.16	8.69	10.55	12.80

The antenna structure is depicted in Fig. 9(b). The radome, comprising a four-layer cascaded FSS configuration, consists of a 12×12 periodic array of heterogeneous unit cells per layer, yielding overall dimensions of 240×240×187 mm^3. Besides, the phase center of the PLPDA feed exhibits frequency-dependent displacement. To mitigate this effect, the phase center at the operational frequency of 5.8 GHz was specifically selected and precisely positioned at the focal point of the radome, with a feed-to-radome distance of F = 86 mm.

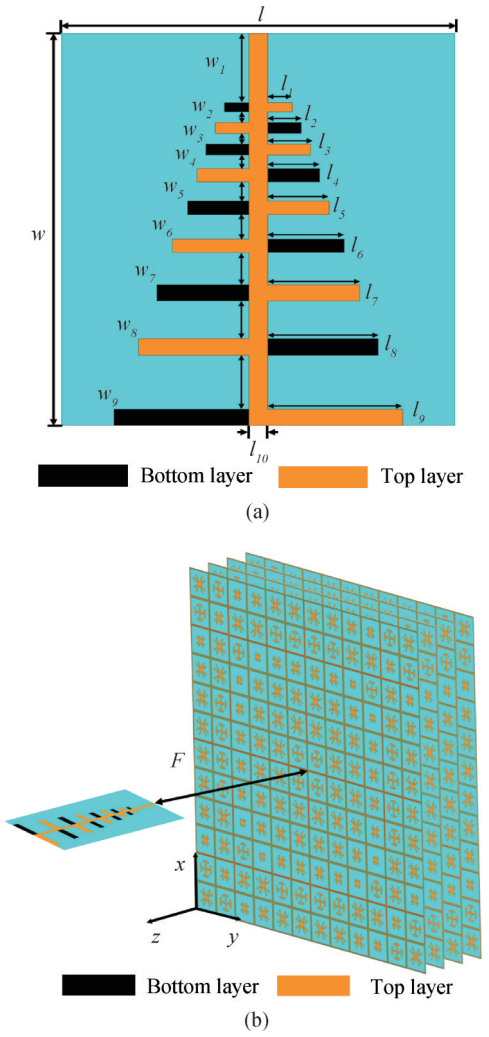

Fig.9 (a) Configuration of PLPDA (b) Structure of the Proposed Antenna

3 Results and Discussion

Full-wave simulations of the antenna structure as shown in Fig. 9(b) were performed by using ANSYS HFSS. As shown in Fig. 10, the radome effectively transforms the spherical wavefront incident from the feed antenna into a quasi-planar wavefront at 5.4 GHz and 5.8 GHz and the 3D radiation patterns at 5.4 GHz and 5.8 GHz are shown in Fig. 11.

To validate the design, the proposed PLPDA and radome were fabricated, with physical prototypes shown in Figs. 12(a) and (b). The radiation patterns and gain were measured in an anechoic chamber, while the S-parameters of the PLPDA were measured by using a vector network analyzer.

Fig. 13(a) shows good agreement between simulated and measured reflection coefficients of the PLPDA, confirming that the measured impedance bandwidth is less than -10 dB over 5 – 6 GHz. Fig. 13(b) compares simulated and measured peak gains for the PLPDA with and without the radome. Results indicate that with the radome, the antenna gain ranges from 10.1 dB to 15.9 dB, achieving a maximum peak gain of 15.9 dB at 5.8 GHz—representing an average gain enhancement of 6.26 dB over the radome-free configuration. Additionally, the design achieves a 3-dB gain bandwidth of 50% (from 5.5 to 6 GHz). Fig. 13(b) also presents the simulated radiation efficiency of the overall antenna with the radome, which remains around 0.8 across the entire operating band, further validating the low transmission loss of the proposed radome design.

To characterize the radiation performance within the operational band, six discrete frequencies (5.03 GHz, 5.2 GHz, 5.4 GHz, 5.6 GHz,5.8 GHz and 5.91 GHz) were selected for analysis. The simulated and measured 2D radiation patterns on the yoz and xoz planes at these

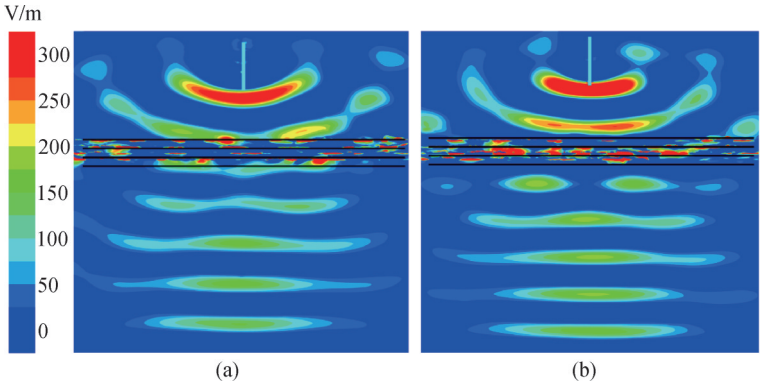

Fig.10 Simulated electric field contours on a cutting surface in the xoz-plane at the frequency of (a) 5.4 GHz and (b) 5.8 GHz

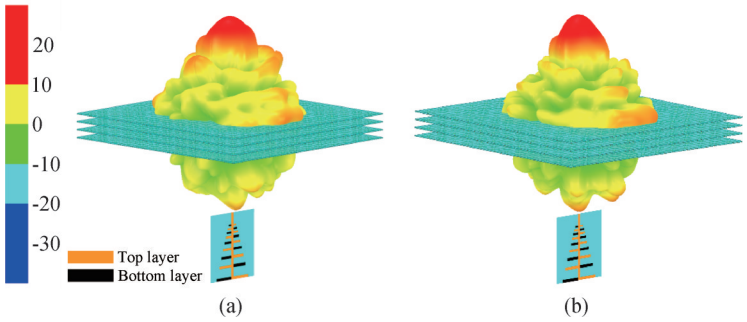

Fig.11 Simulated 3-D radiation pattern at frequency of (a) 5.4 GHz and (b) 5.8 GHz

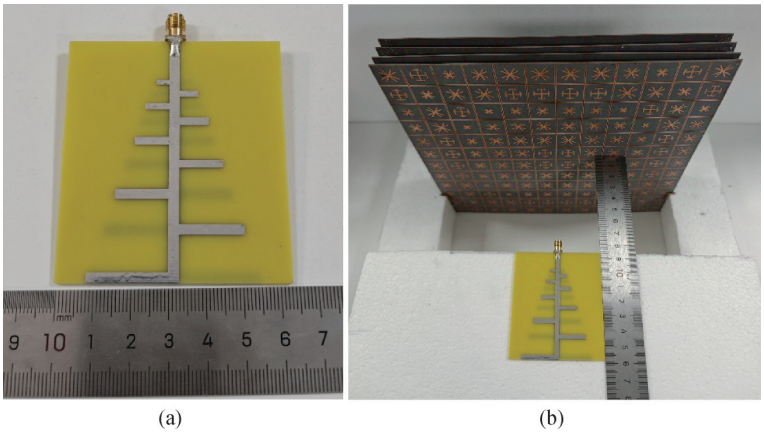

Fig.12 (a) Photograph of the proposed PLPDA (b) Prototype of the presented antenna

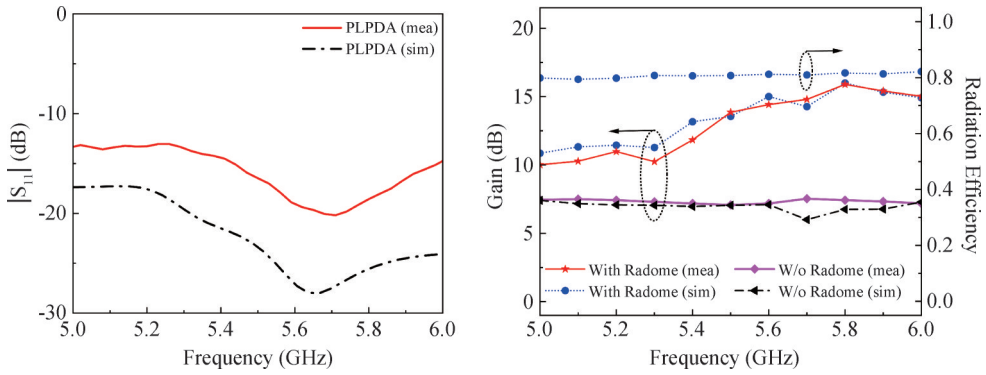

Fig.13 (a) Simulated and measured $|S_{11}|$ of the feed antenna. (b) Simulated and measured peak gains of the PLPDA with and without radome, and Simulated radiation efficiency of the PLPDA with radome

frequencies are compared in Fig. 14, exhibiting good agreement with simulation results. With the radome, the $2\theta_{0.5}$ remains below 23° over 5–6GHz and progressively narrows as frequency increases. At 5.8 GHz, the

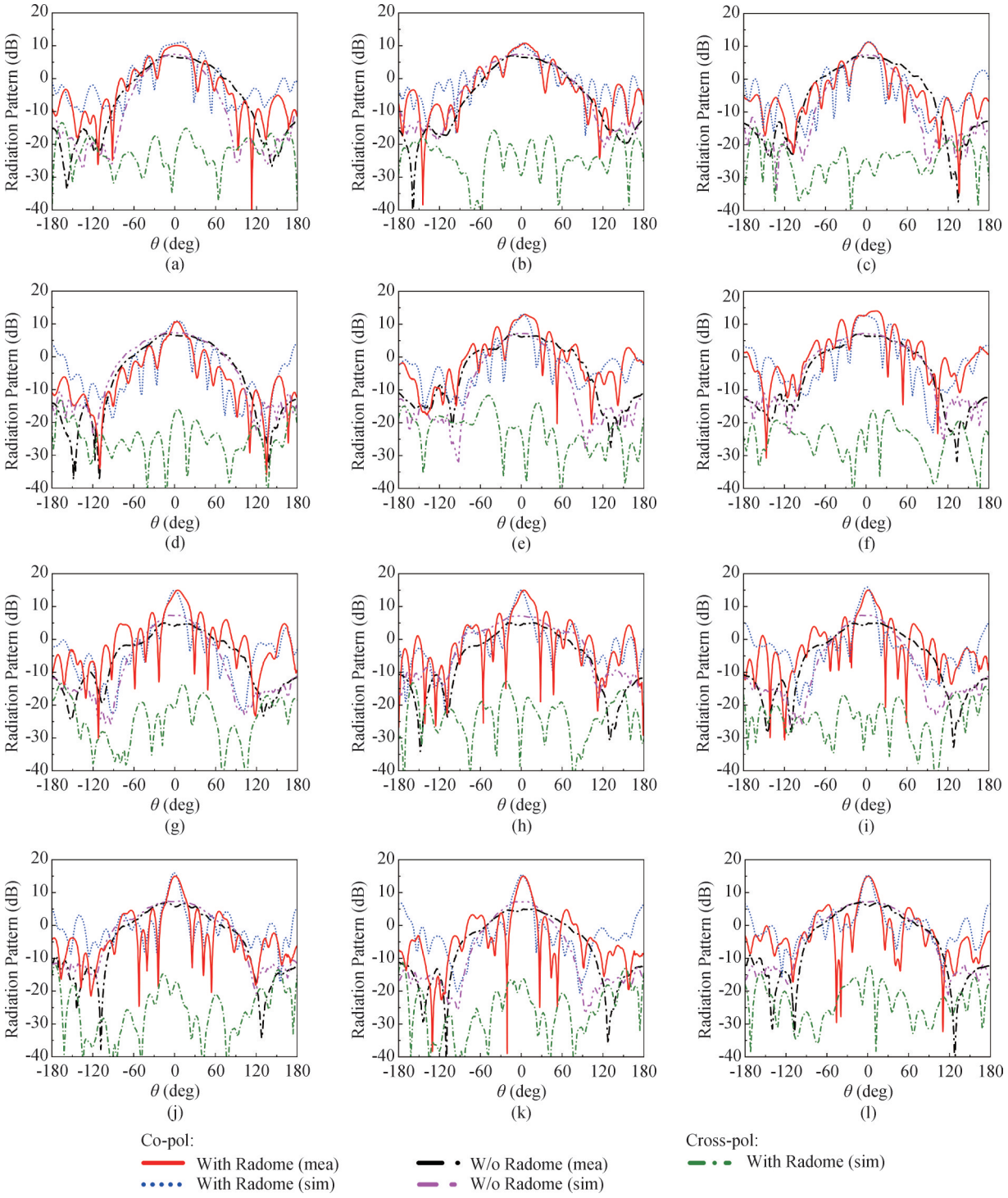

Fig.14 Simulated and measured 2-D radiation patterns of the PLPDA with and without radome
(a), (c) ,(e), (g), (i)and (k) is yoz-plane at 5.03 GHz, 5.2 GHz, 5.4 GHz, 5.6 GHz,5.8 GHz and 5.91 GHz
(b), (d), (f), (h), (j)and (l) is xoy-plane at 5.03 GHz, 5.2 GHz, 5.4 GHz, 5.6 GHz,5.8 GHz and 5.91 GHz

measured $2\theta_{0.5}$ is 16° representing a 73.3% reduction relative to the PLPDA's 60° at the same frequency. Furthermore, the cross-polarization remains below -20 dB across the entire operating band. This confirms enhanced beam energy concentration and superior directivity enabled by the radome.

To quantitatively evaluate the efficiency of the radome in enhancing gain, the Gain-Enhancement- per-Unit-Volume (GEPV) metric is introduced, defined as the ratio of the peak gain difference between the antenna with and without the radome to the radome's volume. Table 2 compares the proposed antenna with other radome-integrated antennas. It can be observed that the proposed antenna achieves a GEPV of 5.21×10^{-6} dB/mm³, which is slightly lower than some reference designs. However, it exhibits superior beamwidth constraint capability, indicated by a narrower $2\theta_{0.5}$, making it more suitable for portable LACS applications.

Table 2 Comparison between proposed and other works

Works	Radome Type	Frequency (GHz)	Peak Gain without Radome(dB)	Peak Gain with Radome(dB)	Radome Size (mm)	GEPV (dB/mm³)	$2\theta_{0.5}$ (Widest/ Narrowest)
[7]	Metamaterial Directors	1.13–1.84 2.11–6	7.3	10	140×90×50	4.29×10^{-6}	53°/20°
[18]	Dielectric Microwave Lens	0.9–10	10.5	15	110×110×15	24.8×10^{-6}	60.9°/29.4°
[19]	FSS	10-14	17	26.7	100×100×15	64.7×10^{-6}	NaN(wide)/25°
Proposed	FSS	5.03–5.91	7.5	15.9	240×240×28	5.21×10^{-6}	23°/16°

4 Conclusion

This paper presents a portable broadband high-gain antenna for UAV low-altitude countermeasures, operating within the RPAS-specific frequency band. The design employs a four-layer cascaded FSS to construct a radome, where the unit cells achieve continuous 360° transmission phase coverage with transmission loss below 1 dB. Measured results demonstrate that the antenna delivers a gain ranging from 10.1 dB to 15.9 dB over 5 – 6 GHz, reaching a peak gain of 15.9 dB at 5.8 GHz, while maintaining the $2\theta_{0.5}$ below 23° throughout the operational band. Compared to existing portable UAV countermeasure systems, the proposed antenna achieves a peak gain improvement of 59% and a 56% reduction in $2\theta_{0.5}$.

Author Contribution:

Bing Yu: Provided guidance on research direction and methodology. Reviewed and critiqued the research design and manuscript at different stages. Xiaoxin Yang: Conceived the research idea and designed the overall framework. Conducted in-depth literature review and formulated research questions. Collected and analyzed the majority of the data. Wrote the main body of the manuscript and led the revision process. Fei Liu: Contributed to the preliminary investigation as a representative from the industry sector. Jiang Shang: Assisted in data collection and organization. Performed preliminary data analysis and contributed to data interpretation. Yan Li: Participated in discussions on research findings and provided valuable feedback for manuscript improvement.

Funding Information:

This research received no external funding

Data Availability:

The authors declare that the main data supporting the findings of this study are available within the paper and its Supplementary Information files.

Conflicts of Interest:

The authors declare no competing interests.

Dates:

Received 28 June 2025; Accepted 05 September 2025; Published online 30 September 2025

References

[1] *Xue, H.* , Zhuo, Z., Yan, W. & Zhang, Y. (**2025**). Research on UAV Jamming Signal Generation Based on Intelligent Jamming. IEEE Access, 13, 14686-14701. doi:https://doi.org/10.1109/ACCESS.2025.3530987.

[2] Li Z., Gao Z., Wang K., Mei Y., Zhu C., Chen L., Wu X. & Niyato, D. **2025**. *Unauthorized UAV Countermeasure for Low-Altitude Economy: Joint Communications and Jamming Based on MIMO Cellular Systems. IEEE Internet of Things Journal*, 12(6), 6659-6672. doi: https://doi. org/10.1109/JIOT.2024.3491796.

[3] Park S., Kim H. T., Lee S., Joo H., & Kim H. (2021). Survey on anti-drone systems: Components, designs, and challenges. IEEE access, **9**, 42635 -42659.

[4] Ghamari M., Rangel P., Mehrubeoglu M., Tewolde G. S., & Sherratt R. S. (2022). Unmanned aerial vehicle communications for civil applications: A review. *IEEE Access*, **10**, 102492-102531. doi: https://doi. org/10.1109/ACCESS.2022.3208571.

[5] Xu Junming, Zhao Guoqing, Liu Aidong. (**2021**) Overview of Development Status of Anti-UAV System at Home and Abroad. *Journal of Ordnance Equipment Engineering* , 42 (S1):5 -8.

[6] Qiu Xiaojian, Luo Boya, Fu Zhen, et al. (**2024**) An overview on development of domestic and foreign anti-UAV technology. *Tactical Missile Technology* , 5,63-73.

[7] Kim I., Lee H. Y., Lee D. M., Lee H. J., Kim H., Kim E. S., & Kim N. Y. (2023). Broadband gain enhanced narrow-beam vivaldi antenna with ring and directors for handheld antidrone jamming system. *IEEE Antennas and Wireless Propagation Letters* , 23(1), 214-218. doi: https://doi. org/10.1109/LAWP.2023.3321899

[8] Wang De - cai, Chen Bo & Feng Mei. **2018**. *A compact portable unmanned aerial vehicle interference antenna. Electronic Design Engineering* , 26(11),100-104.

[9] Xie Fei, Yu Peng, Liu Bodong & Ji Yanlong. **2019**. *Design and implementation of a dual-band dual-feed UAV*

interference antenna. Journal of Terahertz Science and Electronic Information Technolog .17 (04), 589-593.

[10] Wei H., Wang X., Shi X., & Liang B. (2020). Research and experiments on anti-UAV technology. *The Applied Computational Electromagnetics Society Journal (ACES)* ,35(5).

[11] Stoumpos C., Fraysse J. P., Goussetis G., Gonzalez C. G., Sauleau R., & Legay H. (2021). Highly efficient broadband pyramidal horn antenna with integrated H-plane power division. *IEEE Transactions on Antennas and Propagation* , 70 (2), 1499-1504. doi: https://doi. org /10.1109/ TAP.2021.3111276.

[12] Lu K., Leung K. W., & Yang N. (2020). 3-D-printed circularly polarized twisted-ridge horn antenna. *IEEE Transactions on Antennas and Propagation* , 69(3), 1746-1750.doi: https: //doi.org /10.1109/TAP.2020.3031764.

[13] Liu N., Sheng X., Zhang C., & Guo D. (2019). Design and synthesis of band-pass frequency selective surface with wideband rejection and fast roll-off characteristics for radome applications. *IEEE Transactions on Antennas and Propagation* , 68(4), 2975-2983.

[14] Guo M., Zheng Y., Chen Q., Ding L., Sang D., Yuan F., ... & *Fu, Y.* (**2020**). Analysis and design of a high-transmittance performance for varactor- tunable frequency-selective surface. IEEE transactions on antennas and propagation, 69 (8), 4623-4632.

[15] Liu N., Sheng X., Zhang C., & Guo D. (2017). Design of frequency selective surface structure with high angular stability for radome application. *IEEE Antennas and Wireless Propagation Letters* , 17(1), 138-141.

[16] Yu Y. M., Chiu C. N., Chiou Y. P., & Wu T. L. (2014). A novel **2**.5-dimensional ultraminiaturized- element frequency selective surface. *IEEE Transactions on Antennas and Propagation* , 62(7), 3657-3663.

[17] Abdelrahman A. H., Elsherbeni A. Z., & Yang F. (2013). Transmission phase limit of multilayer frequency-selective surfaces for transmitarray designs. *IEEE Transactions on Antennas and Propagation* , 62(2), 690-697.

[18] Hilal A. H., Reja A. H., & Mohammed M. J. (2025). Modify a dual ridge horn antenna for drone jamming applications. *Sensors International* , **100334**.

[19] *Ghaderi, M.* , & Rezaei, P. (**2025**). Analytical design of low-profile wideband multi-layer transmitarray antenna for Ku band. Wireless Networks, 31(2), 1949-1957.

[20] Azari A., Skrivervik A., Aliakbarian H., & Sadeghzadeh R. A. (2023). A super wideband dual-polarized vivaldi antenna for 5G mmWave applications. *IEEE Access* , **11**, 80761-80768. doi: https://doi.org/10.1109/ACCESS.2023.3300040.

[21] *Abdulhameed, A. A.* , & Kubík, Z. (**2022**). Design a compact printed log-periodic biconical dipole array antenna for EMC measurements. Electronics, 11(18), 2877. doi: https://doi. org/ 10.3390 /electronics1118 2877.

[22] Diao W., Li R., Li Y., & Zhang Z. (2024). An ultra-wideband h-plane monopulse log-periodic antenna for jamming signal finding. IEEE Transactions on Antennas and Propagation. **72** (9), 7305-7310. doi: https://doi.org/10.1109/TAP.2024. 3418208.

[23] Guo L., Wang Z., Zeng W., Hou S., Yang Z. & Liu, Y. **2022**. *A compact and high gain metalens antenna based on impedance matching mechanism. AEU - International Journal of Electronics and Communications* , 146, 154113. doi: https:// doi.org/10.1016/j.aeue.2022.154113.

[24] Cai Y., Li W., Li K., Gao S., Yin Y., Zhao L. & Hu, W. **2019**. *A Novel Ultrawideband Transmitarray Design Using Tightly Coupled Dipole Elements. IEEE Transactions on Antennas and Propagation* , 67(1), 242-250. doi: https://doi. org/ 10.1109/TAP.2018.287807 9.

[25] *Liang, J.* , Wu, Z., Li, L. & Huang, Y. (**2024**). A high efficiency wideband co - polarised metalens antenna. IET Microwaves, Antennas & Propagation, 18(11), 803-809. doi: https://doi.org /10.1049/mia2.12517.

[26] *Rao, W., Wang, Y. & Guo, L.* (**2023**). A dual-layer polarisation rotating element for transmitarray designs. IET Microwaves, Antennas & Propagation, 17(9), 758-765. doi: https: //doi.org / 10.1049/mia2. 12386.

[27] Ning Z., Li T., Qing X., Shi J., Li S., Su Y., E., W., *Xue, C.* , Lou, Q. & Hao, Z. (**2023**). Microwave Metalens Antennas. Proceedings of the IEEE, 111(8), 978-1010. doi: https://doi. org/10.1109/JPROC.2023.328 7599.